



## Electrochemical performance of tin-based nano-composite electrodes using a vinylene carbonate-containing electrolyte for Li-ion cells

G. Kilibarda <sup>a,b,\*</sup>, S. Schlabach <sup>a</sup>, V. Winkler <sup>a,b</sup>, M. Bruns <sup>a,c</sup>, T. Hanemann <sup>a,b</sup>, D.V. Szabó <sup>a</sup>

<sup>a</sup> Karlsruhe Institute of Technology, Institute for Applied Materials, Germany

<sup>b</sup> University of Freiburg, Department of Microsystems Engineering, Germany

<sup>c</sup> Karlsruhe Institute of Technology, Karlsruhe Nano Micro Facility, Germany



### HIGHLIGHTS

- Synthesis of tin-based hydrocarbon nanoparticulate composite electrodes.
- Vinylene carbonate in the electrolyte improves the electrochemical performance.
- A polymeric SEI, detected by XPS, is the reason for the improvement.
- The evolution of reactions occurring during cycling are traced by XRD.
- An explanation for different cycling behavior at varying current density and temperature is presented.

### ARTICLE INFO

#### Article history:

Received 21 January 2014

Received in revised form

26 March 2014

Accepted 7 April 2014

Available online 18 April 2014

#### Keywords:

Li-ion cell

Sn nanocomposite electrode

Temperature

Current density

Vinylene carbonate (VC)

SEI-formation

### ABSTRACT

Tin represents a promising material to increase the specific capacity compared to the state of the art graphite anodes in lithium ion cells. The aim of this work is to explain the electrochemical behavior of tin-based hydrocarbon nanoparticulate composite electrodes, synthesized by means of a microwave plasma technique without any binder or slurry process. A comprehensive electrochemical characterization shows that adding vinylene carbonate (VC) to the electrolyte improves the electrochemical performance. Electrochemical impedance spectroscopy (EIS) and *post mortem* investigations of the cycled electrode material by X-ray photoelectron spectroscopy (XPS) reveal the formation of a polymeric SEI during the first cycles, being responsible for the improvement. The differential capacity plots of the discharging process show that the lithium richest phase ( $Li_{22}Sn_5$ ) is formed during electrochemical loading. A comprehensive characterization with specially designed electrochemical tests finally demonstrates the decrease of capacity with increasing temperature. This is due to intensified mechanical stresses and a fresh SEI formation. Due to destruction of the electrode material degradation is also observed with increasing current density. The SEI layer on the surface of the electrodes is confirmed by scanning electron microscopy (SEM) investigations and energy dispersive X-ray spectroscopy (EDS) elemental mapping.

© 2014 Elsevier B.V. All rights reserved.

## 1. Introduction

Owing to their high energy density, long cycle life and environmental safety characteristics, lithium ion cells have taken the most important role in the energy storage. Graphite anodes are

currently state of the art in lithium ion cells with a specific capacity of 372 mAh g<sup>-1</sup>. The demand for materials with higher capacity increases and so today's research is still in search of useful material systems to replace graphite as anode in Li-ion cells. Tin-based materials represent such a promising material [1–3], with a theoretical specific capacity of 994 mAh g<sup>-1</sup> for metallic Sn. Additionally, carbonaceous materials like hydrocarbons, C<sub>x</sub>H<sub>y</sub>, have been reported [4–11], characterized by a specific capacity depending on the H/C ratio. Values of up to 800 mAh g<sup>-1</sup> are commonly reported. Chen et al. [9] are finding specific capacities of about 3400 mAh g<sup>-1</sup>, and Fey et al. [10] even report a specific capacity around

\* Corresponding author: Goran Kilibarda, KIT, Hermann-von-Helmholtz-Platz 1, 76344 Eggenstein-Leopoldshafen, Germany. Tel.: +49 721 608 23702.

E-mail address: [goran.kilibarda@kit.edu](mailto:goran.kilibarda@kit.edu) (G. Kilibarda).

4765 mAh g<sup>-1</sup>. Because the tin-based materials suffer from a huge volume change during cycling and, therefore, a degradation of the specific capacity, the challenge is to keep the promising initial capacities constant for many cycles. The aim of this work is to improve the cyclic stability by targeted materials design. Our approach is to use nanoparticulate composites. We expect such materials to benefit from the nanoporous morphology, featuring locally free space to compensate volume changes during the charging/discharging process, as it was reported elsewhere [12–16]. The targeted synthesis of a nanoparticulate composite material like tin–hydrocarbon should minimize the degradation, as the hydrocarbon can act as a buffering system and also contribute itself to the whole capacity of the composite. Additionally, the additive VC in the electrolyte is able to form an SEI layer, which is more stable comparing to the standard electrolyte without additives. This enhancement of the SEI can also minimize the already mentioned degradation of specific capacity.

The electrochemical investigation was performed on nanoparticulate electrode material, synthesized by means of the Karlsruhe Microwave Plasma Process (KMPP) [17] and deposited onto the Ni current collector directly out of the KMPP particle stream. To investigate the electrochemical performance tailored tests were designed, addressing the main parameters temperature and current density, as well as the additive vinylene carbonate (VC) to the electrolyte. Complementary chemical *post mortem* analysis were performed by X-ray diffraction (XRD) and X-ray photoelectron spectroscopy (XPS) to investigate several reaction steps taking place in the discharging process with respect to the chemical composition of electrode surfaces. These studies are complemented by scanning electron microscopy (SEM) and energy dispersive X-ray spectroscopy (EDS) to get information on the morphology and element distribution as well.

## 2. Experimental

### 2.1. Electrode synthesis and material characterization

The Karlsruhe Microwave Plasma Process was used for the synthesis of electrodes. The principles of the process are described elsewhere [17]. Water free tetra-*n*-butyltin, Sn(C<sub>4</sub>H<sub>9</sub>)<sub>4</sub>, (94%, ABCR, Karlsruhe, Germany) was used as a precursor with a feeding rate of 5 ml h<sup>-1</sup> and pure Ar (99.9999%, Air Liquide, Düsseldorf, Germany) with a gas flow rate of 5 l min<sup>-1</sup> as carrier gas. The power of the microwave was set to 700 W and the system pressure to 12 mbar. These special parameters are expected to yield in nano-composite material consisting of tin-based particles combined with hydrocarbons, C<sub>x</sub>H<sub>y</sub>, stemming from the organic precursor. The presence of the hydrocarbons was shown in previous work [18] using the same organometallic precursor, but Ar–O<sub>2</sub> gas mixture as reaction and carrier gas, yielding in a SnO<sub>2</sub>–C<sub>x</sub>H<sub>y</sub> nanocomposite.

The resulting composite particles were deposited as a porous nanoparticle-film onto 300 °C preheated Nickel current collector substrates, showing good adhesion onto the collector. Thus, additional slurry systems in combination with carbon black or binder are not necessary. Besides the deposition, powder of the composite material was collected by thermophoresis for further characterization. The weight ratios of the composite material were investigated by thermogravimetric analyses coupled with differential scanning calorimetry (TGA–DSC) on a Jupiter STA 449C (Netzsch, Selb, Germany). The samples were treated in synthetic air with a heating rate of 5 K min<sup>-1</sup> from RT to 1000 °C. The material shows a weight ratio of 65 wt% Sn and 35 wt% hydrocarbons. The H/C ratio of the composite material was investigated by HCN analyses on an elemental analyzer for microsamples, LECO CHNS 932 (LECO, Mönchengladbach, Germany). The H/C ratio, including a correction

of water content of 2 wt% (TGA–DSC at 150 °C) was measured to be around 1.6.

### 2.2. Cell assembling

All electrodes were assembled as Swagelok-type half-cells in an argon-filled Unilab glove box (MBraun, Garching, Germany). To reduce moisture, stemming potentially from the synthesis itself and the sample electrode transport into the glove box, respectively, all electrodes were dried in a vacuum oven (Vakucenter VC20, Salvis-Lab, Rotkreuz, Germany) for 2 h at 140 °C. A glass fiber (Whatman, Maidstone, England) was used as separator, and lithium foil (Alfa-Aesar, Ward-Hill, USA) as counter and reference electrode. Two different electrolytes were used. The first electrolyte is a commercially available solution of 1 M LiPF<sub>6</sub> in ethylene carbonate (EC) and dimethyl carbonate (DMC) (50:50) and was obtained from Merck (LP 30, Merck, Darmstadt, Germany). For the second electrolyte, vinylene carbonate (VC) (97%, Sigma Aldrich, St. Louis, USA) was added to the commercial electrolyte. This resulted in a composition of 1 M LiPF<sub>6</sub> in EC, DMC and VC (45:45:10). Prior to the cycling tests all cells were stored for 24 h after assembling to ensure complete wetting of the electrode.

### 2.3. Electrochemical performance

All electrochemical tests were performed using a Lithium cell cycler (LICCY, KIT, IPE, Germany) in a voltage range between 0.1 and 2.8 V vs. Li/Li<sup>+</sup>. Additionally, electrochemical impedance spectroscopy (EIS) was carried out on a Zahner Zennium (Zahner Elektrik, Kronach, Germany) to investigate selected electrochemical reactions in more detail, in particular the SEI formation. For these investigations cells were discharged down to 0.1 V prior to EIS. The frequency used for the impedance measurements was in the range of 100 kHz to 10 mHz and the signal amplitude was set to 5 mV.

Current density and temperature were varied in order to investigate the electrochemical performance of the cells in different environmental conditions. The temperature variation was done by placing the respective half-cells either in a reasonable air-conditioned room (RT), into a drying oven (Heraeus T6060, Thermo-Electron-LED, Langenselbold, Germany), or into a modified conventional refrigerator. Details of the different experimental parameters are summarized in Table 1.

**Table 1**

Investigated half-cells and the corresponding information concerning electrochemical characterization.

Cell	Electrolyte	Active mass (mg)	Temperature (number of cycles)	Current density [mA g <sup>-1</sup> ] (number of cycles)	EIS, after discharge cycle
a	LP30	0.2	RT (50)	41 (50)	–
b	LP30 + VC	0.3	RT (50)	41 (50)	–
c	LP30	0.5	RT (3)	41 (3)	1; 2; 3
d	LP30 + VC	0.3	RT (3)	41 (3)	1; 2; 3
e	LP30 + VC	0.3	RT (60)	41 (15) 82 (10) 164 (10) 821 (10) 41 (15)	–
f	LP30 + VC	0.3	RT (11) 40 °C (10) RT (12) 5 °C (9) RT (8)	41 (50)	–
g	LP30 + VC	0.2	RT (3) 40 °C (1)	41 (4)	2; 3; 4
h	LP30 + VC	0.8	RT (0.5; 2.8 V–0.8 V)	41 (0.5; 2.8 V–0.8 V)	–
i	LP30 + VC	0.7	RT (0.5; 2.8 V–0.25 V)	41 (0.5; 2.8 V–0.8 V)	–

#### 2.4. Targeted electrochemical cycling for post mortem investigations

To investigate the several reaction steps occurring in the discharging process, two electrodes (Table 1, cells (h) and (i)) were synthesized, assembled with VC containing electrolyte and discharged to different specific potentials. The first cell was discharged from 2.8 to 0.8 V, just after the potential where the reduction of  $\text{Sn}^{II}\text{O}$  and the electrolyte is expected, the second one from 2.8 down to 0.25 V, the potential after the expected alloying with lithium.

For the *post mortem* characterization of the electrode material the cycled half-cells were disassembled and rinsed in the glove box using DMC. To avoid atmospheric contact after disassembling, the electrodes were transported in gas tight transfer boxes. In case of XRD a special gas tight sample holder was used, in case of XPS a glove box attached to the instrument was available.

Phase composition of the deposited and dried layers, as well as the cycled layers was evaluated using X-ray diffraction (D8 Advanced, Bruker Corporation, Billerica, USA). To investigate layer morphologies and elemental composition, a field emission scanning electron microscope (FE-SEM, Zeiss Supra 55, Zeiss, Oberkochen, Germany) equipped with an energy-dispersive X-ray spectrometer (EDS, EDAX, AMETEK, Mahwah, USA) was used. The acceleration voltage was set to 2 kV for imaging and 15 kV were used for EDS elemental mapping. The samples were investigated without any sputter-coating. The chemical composition of topmost electrode surfaces was analyzed using X-ray photoelectron spectroscopy (XPS, K-Alpha spectrometer, ThermoFisher Scientific, East Grinstead, UK). Data acquisition and processing using the Thermo Avantage software is described elsewhere [19]. All samples were analyzed using a microfocused, monochromated  $\text{Al K}\alpha$  X-ray source (400  $\mu\text{m}$  spot size). The K-Alpha charge compensation system was employed during analysis, using electrons of 8 eV energy and low-energy argon ions to prevent any localized charge build-up. The spectra were fitted with one or more Voigt profiles (binding energy uncertainty:  $\pm 0.2$  eV). All spectra were referenced to the C 1s peak of hydrocarbon at 285.0 eV binding energy, controlled by means of the well-known photoelectron peaks of metallic Cu, Ag, and Au.

### 3. Results and discussion

Long term cycling data of two cells (Table 1, cells (a) and (b)) with different electrolyte compositions are depicted in Fig. 1. The

starting capacities of both cells are relative comparable to each other. While the cell with LP30 electrolyte shows a pronounced decrease of the specific capacity and large capacity differences between discharge and charge (poor coulombic efficiency) especially for the first 10 cycles, the capacity of the cell with the addition of VC seems to be more constant with coeval better coulombic efficiency. The degradation of this composite material in combination with LP30 was discussed in detail in our previous work [20]. In addition, voltage profiles are shown in Figs. S1 and S2 (Supporting information).

We assume the high capacity values can be attributed to the properties of the composite material consisting of Sn and hydrocarbons. As already mentioned, hydrocarbons exhibit high specific capacities, which depend on the H/C ratio [4–11]. Using the measured H/C ratio of 1.6, a capacity resulting from the hydrocarbon material of around 2450  $\text{mAh g}^{-1}$  can be estimated, when extrapolating data from Zheng et al. [4,5] and Dahn et al. [11] (see Supporting information, Fig. S3). High capacities of the hydrocarbons in the same order of magnitude were already published by Chen et al. [9] and Fey et al. [10], and therefore seem to be realistic. Together with the values of Sn (994  $\text{mAh g}^{-1}$ ) a relative high specific capacity of the composite material can be expected.

Looking at Fig. 1, it can be seen that the tin/hydrocarbon composite in combination with the LP30 + VC electrolyte shows improved electrochemical performance. This finding is supported by the reports of several research groups [21–25], which also show better electrochemical performance of lithium ion batteries when using the additive VC in the electrolyte. These improvements are generally attributed to the advanced properties of the formed SEI [21–25]. This related SEI in VC containing electrolytes seems to be more effective in preventing the electrolyte from an ongoing degradation and therefore does not grow with cycling. Additionally, the impedance of cells is found to be almost invariant at RT upon cycling and the coulombic efficiency and irreversible capacity loss are improved. Auerbach et al. [21] attribute the enhancing influence of VC on the electrochemical performance to the ability of VC to form polymeric surface species during the course of its reduction. Surface films containing polymers are expected to be more cohesive and flexible, and thus provide better passivation properties compared to surface films formed in standard electrolytes without any additives.

The SEI formation of cells containing VC in the electrolyte is investigated in more detail using XPS. The C 1s, O 1s, and Li 1s spectra of the pristine electrode and of the electrodes of two cells cycled down to 0.8 V and 0.25 V (Table 1, cells (h) and (i)), respectively, are shown in Fig. 2.

As already mentioned, and also described by Auerbach et al. [21] and El Ouatani et al. [26], the improved electrochemical performance of VC containing cells can be explained by the ability of VC to form polymeric surface species during the course of its reduction. The components at an exceptionally high binding energy of O 1s = 534.5 eV and C 1s = 291.0 eV seems likely to originate from a VC polymer. According to El Ouatani et al. [26] only the double-bond of VC is polymerized and a ring-opening polymerization of the VC does not take place. The VC polymer obviously is formed during cycling, and its amount is doubled up during the cycling from 0.8 to 0.25 V. However, the exact structure and composition of this polymer still remains an open question. XPS measurements proof, that this polymeric surface species are not formed in a cell without VC. Comparison of the C 1s and O 1s spectra of electrodes cycled with and without VC in the electrolyte is shown in the Supporting information (Fig. S4).

Beside the VC based polymer, XPS proves that the formed SEI also includes further decomposition products of the electrolyte. After discharging from 2.8 to 0.25 V the XPS analysis of the

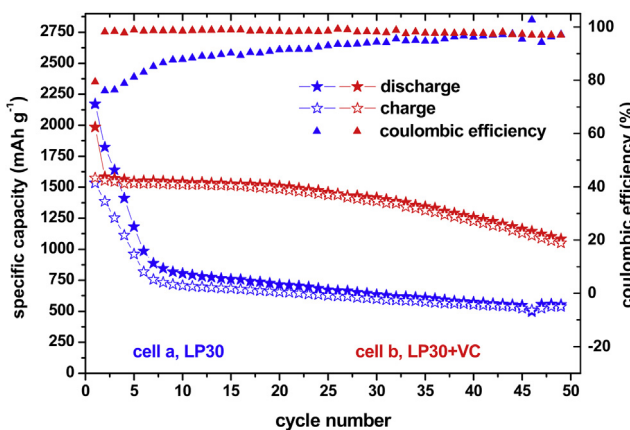


Fig. 1. Comparison of the electrochemical performance of cell (a) with pure LP30 electrolyte and cell (b) with LP30 + VC. For details concerning cells see Table 1. Voltage profiles of the 1st, 3rd, 5th, 10th and 30th cycle of both cells are shown in the Supplementary section (Fig. S1).

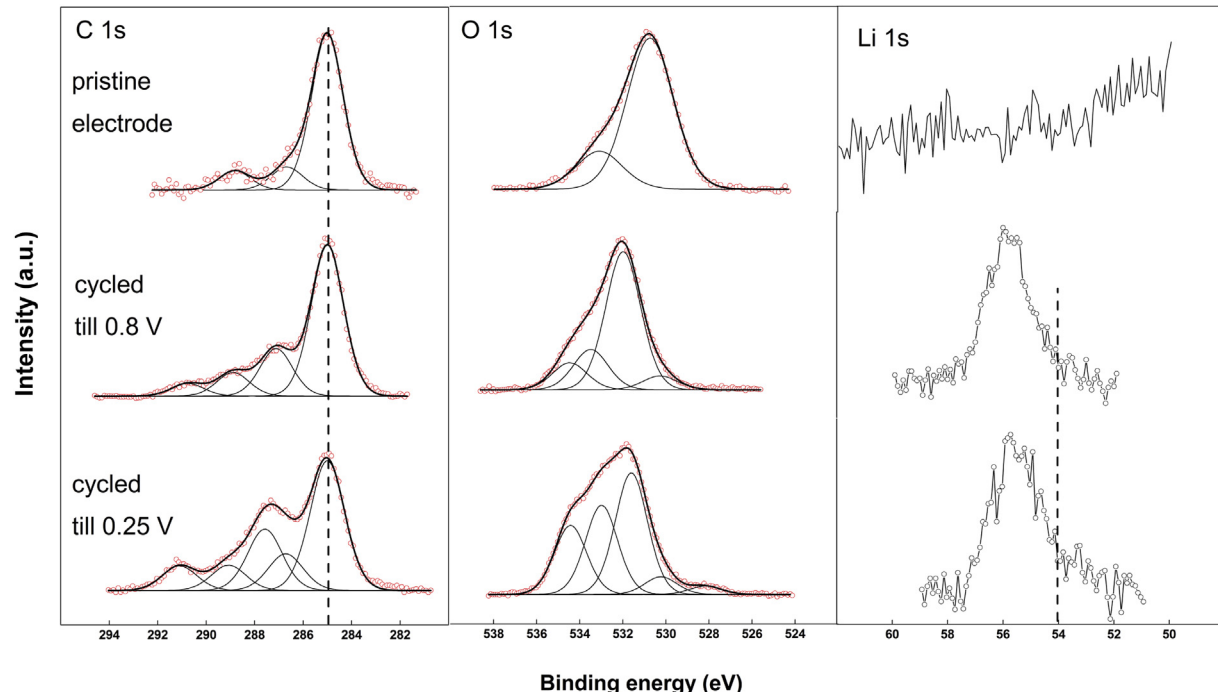


Fig. 2. C 1s, O 1s, and Li 1s XP spectra of a pristine electrode and electrodes cycled to 0.8 V (Table 1, cell (h)) and 0.25 V (Table 1, cell (i)), respectively.

electrode surface shows increasing peak intensities at 286.6 eV, 287.6 eV and 289.0 eV. These peaks appear in addition to the main C 1s component at 285.0 eV of hydrocarbons on pristine electrode surfaces. In a good agreement with literature [27] these components can be attributed to alkoxy-, ethereal-, carbonyl-, and alkyl-carbonate species. The corresponding O 1s peaks, cf. Fig. 2 at 531.6 eV, 532.1 eV and 533.0 eV corroborate these findings [28]. These compounds result from the direct decomposition of the carbonates of the electrolyte (EC, DMC). The additional decomposition of the conducting salt ( $\text{LiPF}_6$ ) is proven by the appearance of peaks ascribed to lithium fluoride (F 1s at 685.1 eV) and several fluorinated lithium phosphate species (F 1s at 687.3 eV, P 2p at 134–137 eV) [28]. The Li 1s spectra of both cycled electrodes in Fig. 2 show a rather broad main peak, containing various lithium species. Due to the low sensitivity for lithium and only slight binding energy shifts between different lithium species this peak was not further deconvoluted. Nevertheless, the Li 1s spectra of both cycled electrodes show a tailing at lower binding energies. This indicates the presence of  $\text{Li}_2\text{O}$  and is also confirmed by the corresponding O 1s component at 528.2 eV [29].

To prove the significant difference of the SEI formation in a cell with pure LP30 electrolyte (Table 1, cell (c)) and VC containing electrolyte (Table 1, cell (d)), EIS results are compared after the first, second and third discharge cycle (Fig. 3). The semicircle at high frequencies within the Nyquist plot is representing the resistance of the SEI [27]. The aim of this measurement is to evaluate SEI related resistance of the 2nd and 3rd cycle compared to the 1st one. For the VC free electrolyte (Fig. 3a) the semicircle is increasing with increasing cycling. The increasing resistance is due to the increasing SEI thickness with cycling. In contrast, a pronounced influence of VC in the electrolyte can be seen in Fig. 3b. The SEI formation occurs only in the first discharging cycle, as no increase of the SEI related semicircle for the following cycles is visible. This behavior is in a good agreement with results from Chen et al. [22].

Within the discharging process of the half-cell, the Sn-based composite electrode material undergoes specific reactions with

both, the electrolyte, and the lithium of the counter electrode occurring at related potentials. To evaluate the involved reactions in more detail, the first, second, and third discharging processes of the cell with VC containing electrolyte (from Fig. 1) are depicted as a differential capacity plot in Fig. 4 (specific capacity  $C_{\text{sp}}$  vs. potential  $U$ ). In this diagram every peak is representing a chemical reaction. Starting at 2 V, the first region of reactions represents the reduction of tin monoxide [30] and electrolyte [31,32] (formation of SEI) according to the reactions



and



Reaction (2) is typically assumed to be irreversible, and is expected in the first discharging process only. In accordance, the respective peak in Fig. 4 is only visible in the first cycle. After this cycle the coulombic efficiency is nearly constant and close to 99% (see also Fig. 1, VC containing electrolyte). All subsequent reactions in the differential capacity plot are representing the alloying of tin and lithium, following the general reaction



Several alloy reactions can be seen in Fig. 4 and are summarized in Table 2 together with the observed potential values. The assignment is based on literature [12,30,33,34]. It can be seen that the lithium richest alloy,  $\text{Li}_{22}\text{Sn}_5$ , was formed.

Following the discharging process, it is assumed, that the reaction after the lithium–tin alloying is attributed to the formation of chemical bonds between hydrocarbons and lithium ( $\text{Li}_x\text{H}_n\text{C}_m$ ). This reaction was described in literature [4,5,8] to occur near 0 V vs.  $\text{Li}/\text{Li}^+$ . While Mabuchi et al. [8] propose that the capacity arise from the insertion of lithium within nanoscopic cavities of the material,

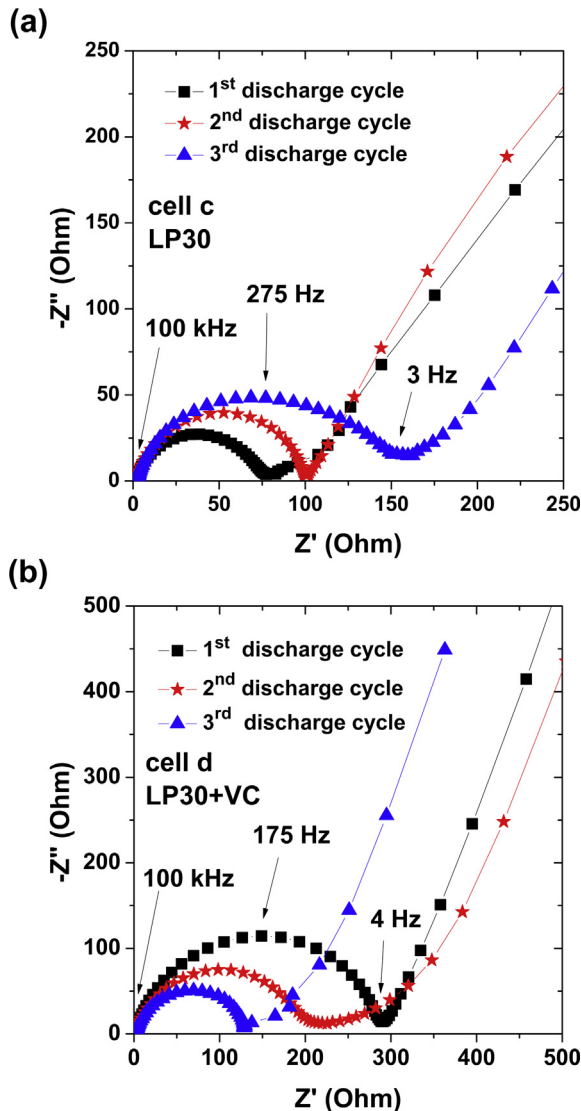


**Fig. 3.** Nyquist plots after the first, second, and third discharge cycle with a) pure LP30 electrolyte and b) VC containing LP30 electrolyte. While the SEI in the pure electrolyte is constantly growing with cycling, in the VC containing electrolyte the SEI formation is completed already after the first cycle.

Zheng et al. [4,5] describe, that the lithium atoms may bind on hydrogen-terminated edges of hexagonal carbon fragments, with local geometries, analogous to the organolithium molecule  $C_2H_2Li_2$ .

To evaluate the involved phases during cycling, X-ray diffraction data of electrodes cycled to three selected potential steps are shown in Fig. 5. The first pattern shows the non-cycled nanoparticle film deposited on Ni substrates, the second pattern shows an electrode cycled from 2.8 down to 0.8 V (Table 1, cell (h)), and finally, the third pattern shows an electrode cycled down to 0.25 V (Table 1, cell (i)). The figure also includes the positions and related intensities for the most expected phases.

For the non-cycled material the occurrence of tetragonal Sn (t-Sn) and tetragonal  $SnO$  is found. Following the discharging process down to 0.8 V the pattern is changing, according to Reaction (1). However, only tetragonal Sn is observed, whereas  $Li_2O$  could not be detected, although the XPS investigation indicates the presences of  $Li_2O$ . One reason might be that the  $Li_2O$  is amorphous or poorly crystallized. Additionally, if  $Li_2O$  is formed as a thin layer around the

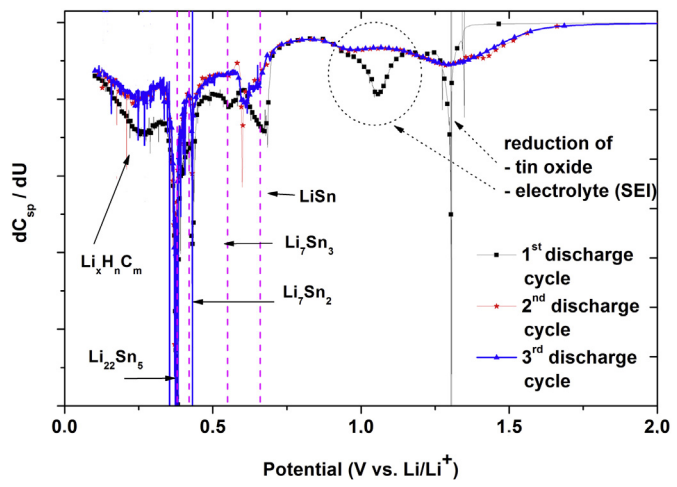


**Fig. 4.** Differential specific capacity plots for the first, second, and third discharging processes of a cell with VC containing electrolyte (Table 1, cell (b)). Each peak represents a chemical reaction.

Sn nanoparticles it will not be detectable using XRD. Further discharging down to 0.25 V causes again changes of the pattern. The electrode at this potential obviously is a mixture of tetragonal Sn and  $LiSn$ , representing the first alloying reaction of Li and Sn. While the differential capacity plot of the discharging process of this cell shows that the lithium richest phase ( $Li_{22}Sn_5$ ) finally is formed (like in Fig. 4), this phase cannot be observed in the XRD measurements. It cannot be excluded that this phase is formed as nano-crystalline material with sizes below the detection limit of XRD. Considering that XRD measurements are performed after destroying the test cells, modifications of the whole system occurring during the disassembling of the cells cannot be excluded. Nevertheless, XRD patterns are showing phase changes during the discharging process and the formation of Li–Sn–alloys.

### 3.1. Influence of the current density on the specific capacity

Although the cycling properties of cells assembled with electrolytes containing the additive VC are promising at a constant and low current density, the influence of the current density on the specific capacity in this electrode system is obvious (Fig. 6). Selected voltage profiles are shown in the Supporting information, Fig. S5. While the current density is increased gradually, gradual decreases in the specific capacity are observed. Moreover, with increasing current density, the inclination of degradation becomes steeper, too. This behavior is found to be most pronounced at a current density of  $821 \text{ mA g}^{-1}$ . After 10 cycles with this current density, the material seems to be damaged strongly. Even after switching back to a current density of  $41 \text{ mA g}^{-1}$  (the current density which actually resulted in predominantly relative constant capacities) degradation and fading of capacities continued, without

**Table 2**

Observed potentials vs.  $Li/Li^+$  and corresponding reactions to tin and lithium alloys.

Potential vs. $Li/Li^+$ (V)	Alloy
0.66	$LiSn$
0.55	$Li_7Sn_3$
0.42	$Li_7Sn_2$
0.38	$Li_{22}Sn_5$

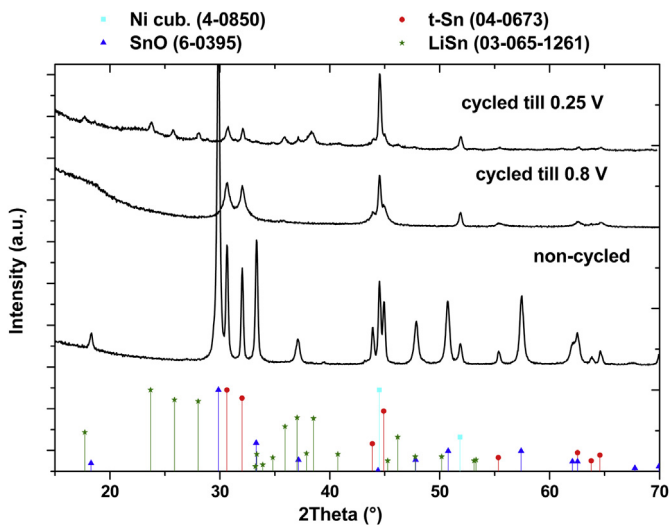


**Fig. 5.** X-ray diffraction patterns of a non-cycled electrode, an electrode cycled from 2.8 down to 0.8 V, and finally an electrode cycled down to 0.25 V. All patterns are compared to JCPDS powder database.

losing good coulombic efficiency. The reason seems to be a destruction of the electrode, as shown by SEM (Fig. 7). The non-cycled electrode shows a homogeneous and crack-free morphology. This can be observed over the whole area and is shown in Fig. 7a. After finishing the cycling measurement, a bulged layer covered with cracks, can be clearly seen in Fig. 7b and c. Cracks can lead to detachment of the material, accompanied by the loss of electronic contact between active particles as well as between active material and the current collector. Therefore, the amount of material which is accessible for lithium storage decreases [12]. It is assumed, that this destruction occur at a current density greater than 164 but less than 821  $\text{mA g}^{-1}$  and is responsible for the following degradation of the specific capacities.

### 3.2. Influence of temperature on specific capacity

The electrochemical performance of cells using VC is dependent on the environmental temperature as well. Fig. 8 illustrates this

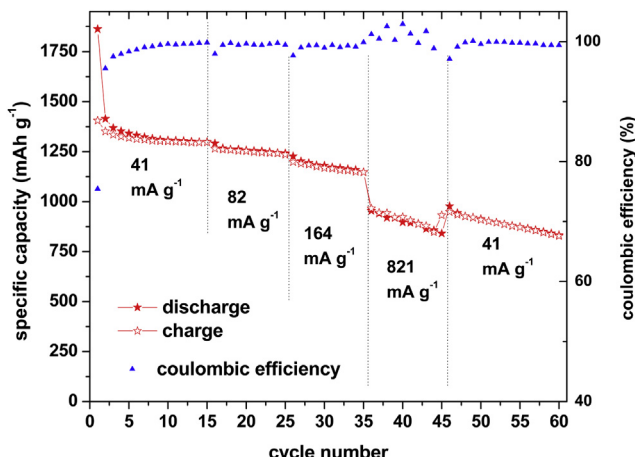


**Fig. 6.** Influence of current density on specific capacity of a cell containing VC in the electrolyte (Table 1, cell (e)). With increasing current density, the specific capacity decreases accompanied by increasing degradation. Voltage profiles of the 1st, 5th, 10th, 20th, 30th, 36th, 38th, 40th and 50th cycle are shown in the Supplementary section (Fig. S5).

behavior. Selected voltage profiles are shown in the Supporting information, Fig. S6. For the first treatment at RT, a relative constant capacity behavior can be observed in agreement with Fig. 1 (LP30 + VC). Increasing the temperature from RT to 40 °C causes a discrete capacity increase, but with ongoing cycling the degradation is becoming steeper. The initial increase of specific capacity can be explained with a combination of reasons. The electrical and the ionic conductivity of the electrolyte increase, respectively [35,36]. At higher temperatures the viscosity of the electrolyte decreases, so with increasing mobility of the ions the capacities increase. Furthermore, the gradient of overpotentials (ohmic and diffusion) is changing drastically when changing the environmental temperature. The overpotential (drop of potential) decreases with increasing environmental temperature. Consequently, the potential of the cell increases, resulting in a specific capacity increase. An explanation of this initial increase of specific capacity due to temperature increase can be found in more detail in our previous work [37].

With higher capacities at 40 °C (11th cycle ca. 1435  $\text{mAh g}^{-1}$  compared to ca. 1587  $\text{mAh g}^{-1}$  in the 13th cycle) it can be assumed, that more  $\text{Li}^+$ -ions are introduced in the electrode. It is known, that the introduction of  $\text{Li}^+$ -ions causes huge volume changes in the Sn material [38]. Consequently, the higher amount of  $\text{Li}^+$ -ions, resulting from increased  $\text{Li}^+$  mobility with temperature, increases the volume change compared to RT, resulting in huge loss of active material and hence decreased capacity for the following cycles.

Additionally, at 40 °C enhanced electrolyte reduction (SEI formation) takes place [39]. This phenomenon is visible in Fig. 9a, showing the differential capacity diagram of the 11th cycle (RT), the 13th cycle (40 °C), and the 23rd cycle (again RT). The potential range was set from 2 to 0.75 V, the region where the SEI formation is expected. After switching the temperature to 40 °C, an additional peak in the region between 1.5 and 1 V appears. This region is believed to be connected to the reduction of electrolyte (SEI formation). With switching the environmental temperature back to RT, the peak according to SEI formation in Fig. 9a (23rd cycle) disappears. Coevally, the coulombic efficiency rises to the same value as for the previous treatment at RT. According to this, the SEI is not continuously formed at RT and consequently the capacities should not degrade much. But, with ongoing cycling the specific capacities degrade even at RT. The pretreatment at 40 °C seems to have already destroyed the electrode to a certain extent. Switching to 5 °C, the capacities are becoming smaller and the same degradation as before can be observed. The initial decrease of the specific capacity can be attributed to the decrease of the electrical and the ionic conductivity and also to the increase of the overpotentials at 5 °C. Surprisingly, at 5 °C a strong decrease of coulombic efficiency in combination with very fluctuating values can be observed. Fig. 9b shows a differential capacity plot of the 33rd cycle (RT) and the 34th cycle (5 °C). It can be seen that the poor coulombic efficiency at 5 °C cannot be attributed to the SEI formation, as no additional peak of the reduction of electrolyte appears at 40 °C, as shown e.g. in Fig. 9a.

The influence of temperature on the electrochemical performance of this material in combination with the electrolyte LP30 was reported in previous work [37]. Looking at 0 °C the coulombic efficiency is nearly at 100%. The observed poor coulombic efficiency in combination with fluctuating values at 5 °C in Fig. 8 must be attributed to VC. Comparable investigations without VC presented in Ref. [37] show a coulombic efficiency around 100%. One reason might be that the melting point of VC is close to 19 °C (given compound specification), and so the viscosity of the electrolyte might change at 5 °C. The switching again to RT causes a little discrete capacity increase but the fading trend could not be detained.

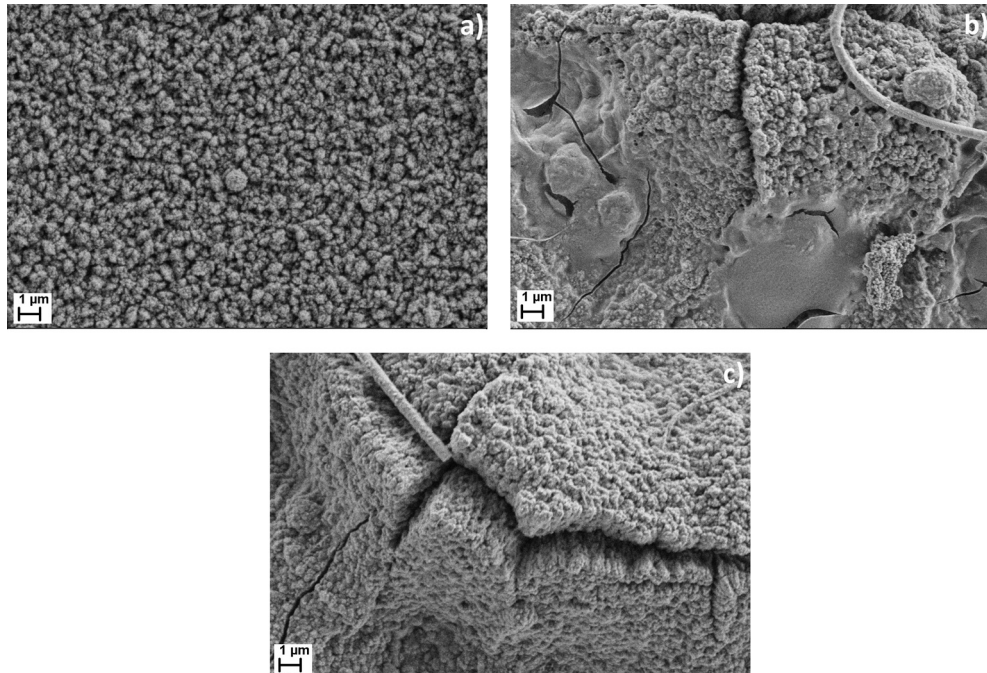


**Fig. 7.** SEM characterization of electrode surfaces before (a) and after finishing the cyclic measurement (b, c). Large destruction of the bulged electrode layer covered with cracks can clearly be seen. It is assumed, that this destruction is responsible for the degradation of the specific capacities.

To confirm the enhanced electrolyte reduction (SEI formation) at elevated temperatures, EIS was performed with a new cell after cycling (Table 1, cell g). The resulting semicircles in the Nyquist plot (Fig. 10) are representing the resistance of the SEI. It can be seen, that the semicircles for both cycles at RT (discharging cycle 2 and 3) are smaller than for the cycle at 40 °C (discharging cycle 4). Hence, the resistance of SEI at 40 °C is larger compared to that at RT, representing enhanced electrolyte reduction (SEI formation) at elevated temperatures. With continuous cycling at elevated temperature the repetitive formed SEI may penetrate into pores of the electrode and in addition may also penetrate into pores of the separator. This may result in a decrease of accessible surface area due to this continuous SEI formation [39].

In summary, at elevated temperature huger volume changes and also enhanced SEI formation takes place. With diminishing the amount of active material and also the accessibility of the electrode in combination with increasing impedance, less  $\text{Li}^+$ -ions can be stored, resulting in a degradation of specific capacity for the following cycles.

To have an optical proof of the SEI, a cell was characterized by SEM after finishing the cycling experiments (Table 1, cell f). Fig. 11 shows the cross section SEM-image of this electrode. In the regions near the surface, a layer exhibiting different morphology in comparison to the rest of the film is clearly visible. This thin film is assumed to be the SEI-layer.

EDS elemental mapping (Fig. 12) shows the elemental composition of two different electrodes. A non-cycled electrode is compared with the electrode after finishing the temperature-cycling measurement (Table 1, cell f). The cross section view of the non-cycled electrode is obtained by scratching the layer with a blade after synthesis. The cross section view of the cycled electrode was possible without further manipulation, because some regions of the film cracked and some pieces were split out. The elemental maps are superimposed images of the analyzed elements Sn, Ni, O and C, respectively. In the pristine composite electrode the elements Sn, C, and O are homogenously distributed. Additionally, Ni, stemming from the current collector, is found in regions without any electrode material.

For the cycled electrode the result is somehow different. The element Sn is predominantly found only in the cross section of the film. Inside the cracks, which are distributed on the surface, only Sn and Ni are detectable, whereas the surface of the film is predominantly consisting of C and O. This can be taken as a proof of a cover layer on top of Sn and Ni, where Sn is representing the electrode material and Ni the current collector. In accordance to the XPS measurements, the assumption of a C and O containing SEI layer on the surface of the electrode is confirmed by SEM investigations and EDS-elemental mapping.

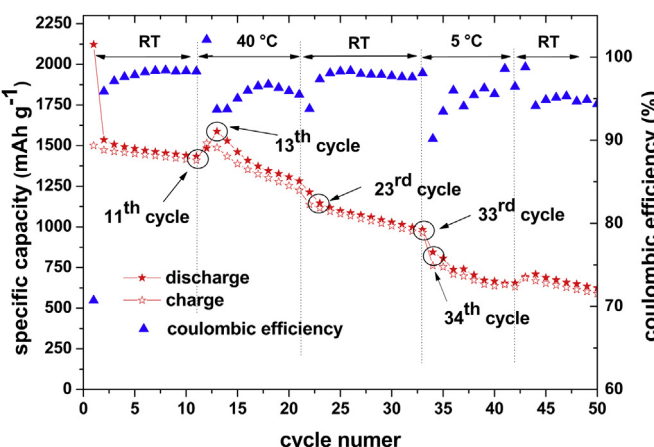


**Fig. 8.** Long term cycling measurement under different thermal conditions of a cell containing VC in the electrolyte. Voltage profiles of the 1st, 5th, 13th, 30th and 37th cycle are shown in the Supplementary section (Fig. S6).

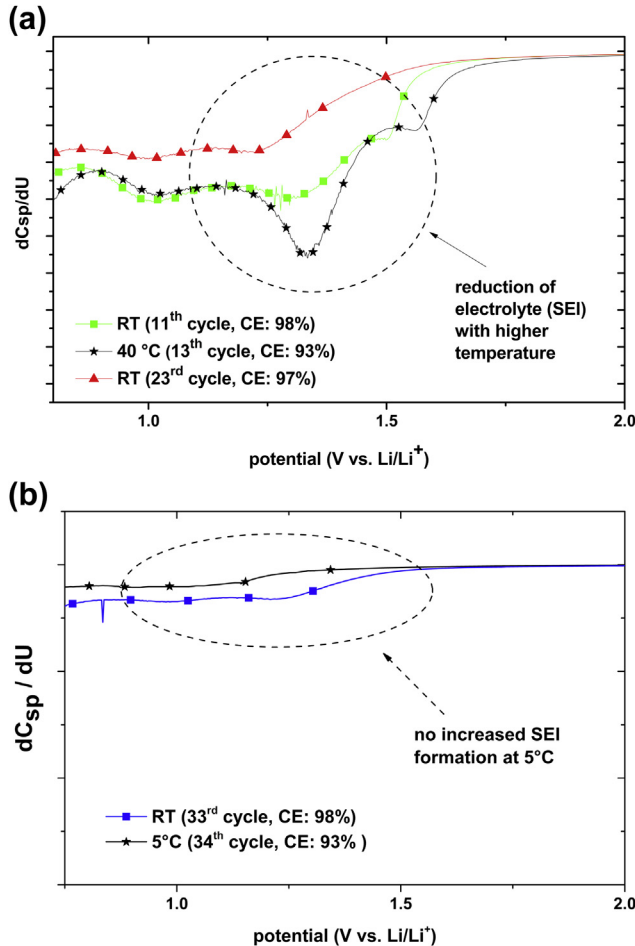


**Fig. 9.** Differential capacity plots (a) extracted from cycling data of the 11th, 13th and 23rd cycles and (b) extracted from the 33rd and 34th cycles, respectively. The potential range was set between 2 and 0.75 V, corresponding to the region of expected SEI formation.

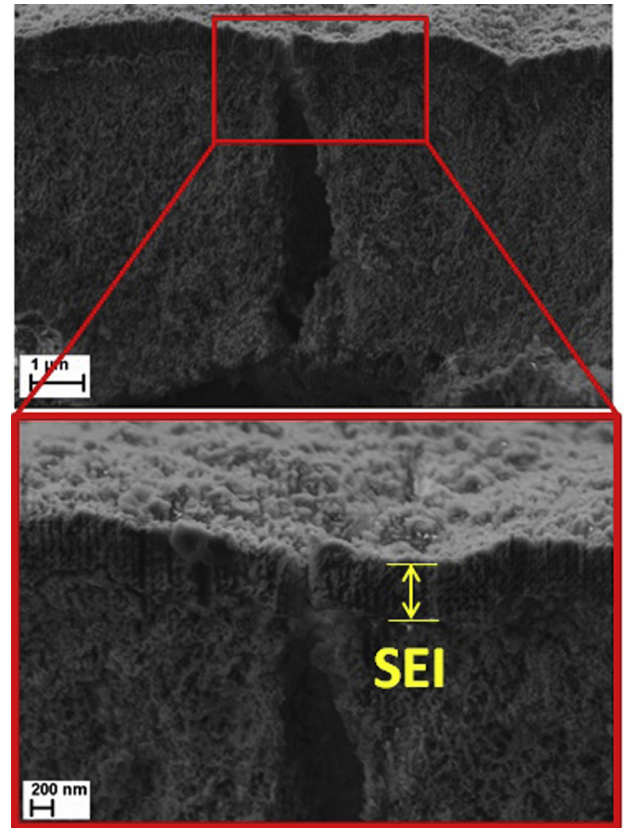


**Fig. 11.** Cross sectional SEM image of the temperature-cycled Sn composite electrode after cycling (Table 1, cell (f)).

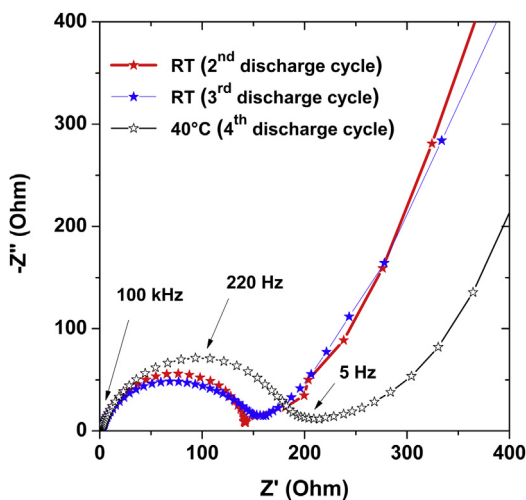


**Fig. 10.** Nyquist plot of EIS measurements at RT (2nd and 3rd cycle) and at 40 °C (4th cycle) of a cell containing VC in the electrolyte. At higher temperature the semi-circle in the Nyquist plot is becoming large, meaning the resistance of the SEI increases. This is a direct proof of enhanced electrolyte reduction and SEI formation.

#### 4. Summary and conclusion

In this work a comprehensive electrochemical characterization of tin-based and hydrocarbon containing nano-composite electrodes for Li-ion cells was presented. The high specific capacities of this material can be attributed to the presence of hydrocarbons with an H/C ratio around 1.6. It was shown, that the additive VC in the electrolyte improves the cycling performance, due to improved SEI formation. XPS measurements led to the conclusion, that a VC based polymer is produced during cycling. Moreover, XPS investigations proved that the formed SEI additionally consists of compounds originating from the decomposition of the electrolyte, and the conducting salt as well. Variation of temperature during the cycling demonstrated, that enhanced temperature enlarges the specific capacity, but also the degradation. Additionally, when increasing the current density, the capacity decreases. The best electrochemical performance could be obtained using VC in the electrolyte, and cycling at RT with a current density below 164 mA g<sup>-1</sup>. In agreement with XPS measurements, EDS measurements showed that the SEI layer contains C and O. XRD revealed the non-cycled electrode to be a mixture of tetragonal Sn and SnO. By crossing the potential of 0.8 V only metallic Sn according to the reduction of SnO and by crossing the potential of 0.25 V a mixture of metallic Sn and LiSn according to the lithium–tin-alloying reaction could be detected.

In conclusion, a good electrochemical performance of the tin-based-hydrocarbon electrode material can be expected using a VC containing electrolyte, current densities below 164 mA g<sup>-1</sup>, and RT as operating temperature.

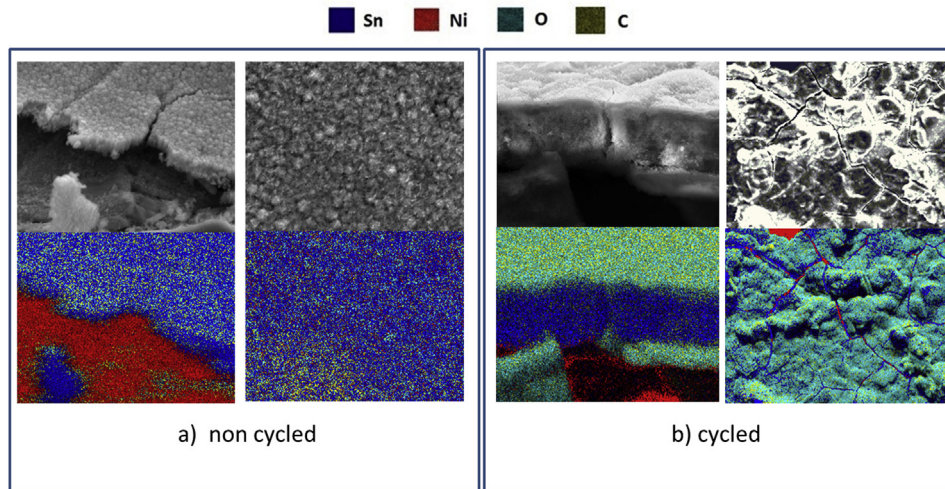


**Fig. 12.** EDS elemental mapping of a cross section and top view of (a) a non-cycled electrode and (b) of a cycled electrode (Table 1, cell (f)).

## Acknowledgments

The authors acknowledge support from B. Bergfeldt (Karlsruhe Institute of Technology, Institute for Technical Chemistry) for H/C analysis and C. Odemer (Karlsruhe Institute of Technology, Institute for Applied Materials) for TGA–DSC analysis.

## Appendix A. Supplementary data

Supplementary data related to this article can be found at <http://dx.doi.org/10.1016/j.jpowsour.2014.04.030>.

## References

- [1] Y. Idota, T. Kubota, A. Matsufuji, Y. Maekawa, T. Miyasaka, *Science* 276 (1997) 1395–1397.
- [2] A.R. Kamali, D.J. Fray, *Rev. Adv. Mater. Sci.* 27 (2011) 14–24.
- [3] M. Wachtler, J.O. Besenhard, M. Winter, *J. Power Sources* 94 (2001) 189–193.
- [4] T. Zheng, Y. Liu, E.W. Fuller, S. Tseng, U. von Sacken, J.R. Dahn, *J. Electrochem. Soc.* 142 (1995) 2581–2590.
- [5] T. Zheng, W.R. McKinnon, J.R. Dahn, *J. Electrochem. Soc.* 143 (1996) 2137–2145.
- [6] S. Yata, Y. Hato, H. Kinoshita, N. Ando, A. Anekawa, T. Hashimoto, M. Yamaguchi, K. Tanaka, T. Yamabe, *Synth. Met.* 73 (1995) 273–277.
- [7] K. Sato, M. Noguchi, A. Demachi, N. Oki, M. Endo, *Science* 264 (1994) 556–558.
- [8] A. Mabuchi, K. Tokumitsu, H. Fujimoto, T. Kasuh, *J. Electrochem. Soc.* 142 (1995) 1041–1046.
- [9] W. Chen, Z. Zhu, S. Li, C. Chen, L. Yan, *Nanoscale* 4 (2012) 2124–2129.
- [10] G.T.-K. Fey, D.C. Lee, Y.Y. Lin, T.P. Kumar, *Synth. Met.* 139 (2003) 71–80.
- [11] J.R. Dahn, T. Zheng, Y. Liu, J.S. Xue, *Science* 270 (1995) 590–593.
- [12] M. Winter, J.O. Besenhard, *Electrochim. Acta* 45 (1999) 31–50.
- [13] Y.-C. Chen, J.-M. Chen, Y.-H. Huang, Y.-R. Lee, H.C. Shih, *Surf. Coat. Technol.* 202 (2007) 1313–1318.
- [14] Y. Wang, J.Y. Lee, *J. Power Sources* 144 (2005) 220–225.
- [15] C. Kim, M. Noh, M. Choi, J. Cho, B. Park, *Chem. Mater.* 17 (2005) 3297–3301.
- [16] H. Li, Z. Wang, L. Chen, X. Huang, *Adv. Mater.* 21 (2009) 4593–4607.
- [17] D. Vollath, D.V. Szabó, *J. Nanopart. Res.* 8 (2006) 417–428.
- [18] D.V. Szabó, G. Kilibarda, S. Schlabach, V. Trouillet, M. Bruns, *J. Mater. Sci.* 47 (2012) 4383–4391.
- [19] K.L. Parry, A.G. Shard, R.D. Short, R.G. White, J.D. Whittle, A. Wright, *Surf. Interface Anal.* 38 (2006) 1497–1504.
- [20] G. Kilibarda, D.V. Szabó, S. Schlabach, V. Winkler, M. Bruns, T. Hanemann, *J. Power Sources* 233 (2013) 139–147.
- [21] D. Aurbach, K. Gamolsky, B. Markovsky, Y. Gofer, M. Schmidt, U. Heider, *Electrochim. Acta* 47 (2002) 1423–1439.
- [22] L. Chen, K. Wang, X. Xie, J. Xie, *J. Power Sources* 174 (2007) 538–543.
- [23] J.C. Burns, N.N. Sinha, D.J. Coyle, G. Jain, C.M. VanElzen, W.M. Lamanna, A. Xiao, E. Scott, J.P. Gardner, J.R. Dahn, *J. Electrochem. Soc.* 159 (2012) A85–A90.
- [24] Y. Hu, W. Kong, H. Li, X. Huang, L. Chen, *Electrochim. Commun.* 6 (2004) 126–131.
- [25] K. Abe, H. Yoshitake, T. Kitakura, T. Hattori, H. Wang, M. Yoshio, *Electrochim. Acta* 49 (2004) 4613–4622.
- [26] L. El Ouatani, R. Dedryvère, C. Siret, P. Biensan, S. Reynaud, P. Iratcabal, D. Gonbeau, *J. Electrochem. Soc.* 156 (2009) A103–A113.
- [27] K. Dokko, Y. Fujita, M. Mohamedi, M. Umeda, I. Uchida, J.R. Selman, *Electrochim. Acta* 47 (2001) 933–938.
- [28] V. Etacheri, O. Haik, Y. Goffer, G.A. Roberts, I.C. Stefan, R. Fasching, D. Aurbach, *Langmuir* 28 (2011) 965–976.
- [29] K. Edström, M. Herstedt, D.P. Abraham, *J. Power Sources* 153 (2006) 380–384.
- [30] R.A. Huggins, *Solid State Ionics* 113–115 (1998) 57–67.
- [31] H. Liu, D. Long, X. Liu, W. Qiao, L. Zhan, L. Ling, *Electrochim. Acta* 54 (2009) 5782–5788.
- [32] M. Marciniek, L.J. Hardwick, T.J. Richardson, X. Song, R. Kostecki, *J. Power Sources* 173 (2007) 965–971.
- [33] R.A. Huggins, in: *Handbook of Battery Materials, Lithium Alloy Anodes*, Wiley-VCH Verlag GmbH, 2007, pp. 359–381.
- [34] J. Wang, I.D. Raistrick, R.A. Huggins, *J. Electrochem. Soc.* 133 (1986) 457–460.
- [35] S.S. Zhang, K. Xu, T.R. Jow, *Electrochim. Commun.* 4 (2002) 928–932.
- [36] P.E. Stallworth, J.J. Fontanella, M.C. Wintersgill, C.D. Scheidler, J.J. Immel, S.G. Greenbaum, A.S. Goetz, *J. Power Sources* 81–82 (1999) 739–747.
- [37] G. Kilibarda, D.V. Szabó, S. Schlabach, T. Hanemann, *Int. J. Electrochem. Sci.* 8 (2013) 6212–6219.
- [38] B.A. Boukamp, G.C. Lesh, R.A. Huggins, *J. Electrochem. Soc.* 128 (1981) 725–729.
- [39] J. Vetter, P. Novák, M.R. Wagner, C. Veit, K.C. Möller, J.O. Besenhard, M. Winter, M. Wohlfahrt-Mehrens, C. Vogler, A. Hammouche, *J. Power Sources* 147 (2005) 269–281.